URSI GASS 2020, Rome, Italy, 29 August - 5 September 2020

Performance assessment of microwave tomography and radar imaging using an anthropomorphic brain phantom

Olympia Karadima*, Navid Ghavami, Ioannis Sotiriou, and Panagiotis Kosmas
Faculty of Natural and Mathematical Sciences, Kings College London
London WC2R 2LS, United Kingdom

Abstract

The use of microwave imaging for brain stroke detection has attracted growing interest in the past decade, inspired by the presence of differences in the dielectric properties of stroke and the surrounding brain tissues. This paper presents and discusses the reconstruction results from measurements on a 3D-printed anthropomorphic head model, containing a cylindrical target simulating the bleeding during a haemorrhagic stroke. To perform the measurements, the head model was immersed inside a purpose-built imaging tank containing a 90% Glycerol matching liquid, and image reconstruction has been obtained both through a DBIM-TwIST tomography algorithm and a Huygens based radar algorithm. Imaging results show that the target can be detected and localized accurately through both algorithms.

1 Introduction

Brain stroke is a severe situation that arises when the blood supply in a part of the brain is either blocked (ischemic) or burst (haemorrhagic). The abnormal blood and oxygen levels lead to the necrosis of the damaged area, with serious consequences to patients' health. Therefore, early diagnosis and treatment of the stroke is critical. Treatment is dependent, among other factors, on the type of the stroke, and thus an incorrect diagnosis could prove lethal for the patient [1]. Consequently, there is a high demand for quick, low-cost and safe imaging methods that are able to detect the stroke as soon as possible, even from the ambulance stage.

Microwave imaging (MWI) is based on the dielectric difference between healthy and diseased tissues. The use of frequencies that are not related to health risks, user-friendly and transportable design as well as the cost-effectiveness of the MWI prototypes are the main reasons that have initiated MWI as an auspicious imaging method than can be used before or in parallel with magnetic resonance imaging (MRI) or computed tomography (CT) scans [2]. MWI imaging systems for brain imaging are divided into tomographic and radar techniques. The first ones rely on solving a non-linear, electromagnetic scattering problem by approximating the dielectric contrast between the known and unknown tissues properties [3]. Radar-based techniques on the other hand solve a simpler problem of discovering the scattering map based on the existing contrast amongst the dielectric properties of brain tissues.

A well-grounded MWI prototype should be optimized both in terms of hardware and algorithm. In [4], the design of a MWI device was analyzed to determine the optimal number of antennas, frequency range and the dielectric properties of the matching medium. Algorithm-wise, the high complexity of the problem raises the need for robust and sufficient methods, while maintaining a low computational cost. Our previous works in [5]-[7] have shown promising results when using the distorted Born iterative method (DBIM) combined with a two-step iterative shrinkage/thresholding method (TwIST), as well as with Huygens algorithm.

The remainder of the paper is organized as follows. Section 2 given a brief description of the employed tomographic and radar-based algorithms. The experimental setup and the phantom preparation procedure are explained in section 3. Measurement results and presented and discussed in section 4, while section 5 concludes the paper and highlights some of the research works planned for the future.

2 Methodology

2.1 DBIM-TwIST tomography algorithm

The DBIM solves the non-linear electromagnetic inverse scattering problem by approximating the total electrical field under the Born approximation:

$$\begin{aligned} E_s(r_n, r_m) &= E(r_n, r_m) - E_b(r_n, r_m) \\ &= \omega^2 \mu \int_V G_b(r_n, r) E_b(r, r_m)(\varepsilon(r) - \varepsilon_b(r) dr) \end{aligned} \tag{1}$$

where E, E_s and E_b are the total, scattered, and background fields, and r_n, r_m indicate transmitter and receiver positions, respectively. The function $(\varepsilon(r) - \varepsilon_b(r))$ denotes the contrast between the complex permittivity of the unknown region and the known background [8]. The resulting linear problem is still ill-posed, therefore the TwIST method [9] is used. At each DBIM iteration, the dielectric contrast function is estimated and is added to the background profile which is then used for calculating the new background

electrical field. To apprehend the dispersive behavior of the materials we apply the first-order Debye model:

$$\varepsilon_s(\omega) = \varepsilon_\infty + \frac{\Delta\varepsilon}{1+j\omega\tau} + j\frac{\sigma_s}{\omega\varepsilon_0} \tag{2}$$

where ε_∞, $\Delta\varepsilon$ and σ_s are the three parameters which are updated at each iteration. The Debye parameters are reconstructed and thus they are used to determine the complex permittivity inside the reconstruction domain [5], [8].

2.2 Huygens based radar algorithm

The Huygens principle based algorithm used here was first introduced in [10], and has previously shown promising preliminary results for other medical applications [11]. The algorithm measures the external surface field of the object and virtually back-propagates it into the imaging domain, reconstructing the internal field within the object as:

$$E_{\mathrm{HP}}(\rho, m, f) = \sum_{n=1}^{N} E_{nm}(f) G(k|\rho_n - \rho|) \tag{3}$$

where E_{nm} is the field received from transmitter m at receiver n, $G(k|\rho_n - \rho|)$ represents the Green function as defined in [10] at each location ρ, and k is the wave number of the medium (90% Glycerol) at frequency f. The algorithm then calculates the resulting intensity image through incoherent summation of the signals from all frequency points and all transmitting positions.

3 Experimental configuration

The measurements in this paper were performed using a purpose-built microwave imaging tank, compatible with both tomography and radar measurement configurations. The setup includes a cylindrical tank with a diameter of 300 mm, which is shielded using an RF absorbing sheet (Laird ECCOSORB AN absorber). The transmitter and receiver antennas are placed in a circular ring inside the acrylic tank (figure 1). Horizontal and vertical mounts allow us to control the antenna positions with accurate precision. The antennas are connected to a multiport Keysight M9019A Vector Network Analyzer (figure 1).

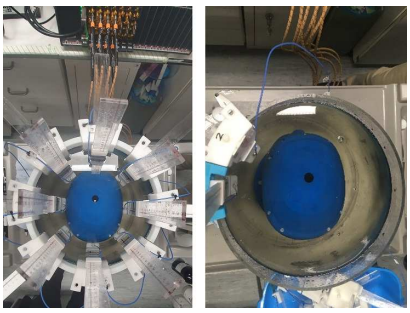

Figure 1. Measurement hardware and setup for tomography (left), and radar (right).

In this work, two different sets of custom-made antennas were tested through measurements. First, spear-shaped antennas (figure. 2(a)), designed on a 28.42 mm by 18.25 mm FR-4 with a spear shape patch fed by a transmission line were used [12]. Then, 5 days later, the measurements were repeated using inverted triangular patch antennas [13]. The triangular antennas have been designed on a 12 mm by 15 mm FR-4 substrate (figure 2(b)).

(a) (b)

Figure 2. Images and dimensions of (a) spear, and (b) triangular antenna.

Different antenna configurations were used for the tomographic and the radar-based measurements. For the case of tomography, an eight-antenna elliptical array was immersed inside the tank. The eight antennas acted both as transmitters and receivers, creating an 8×8 scattering matrix which was fed into DBIM-TwIST. On the other hand, the radar measurement made use of only 2 antennas, one acting as the receiver and the other as transmitter. For each radar measurement, the position of the receiver antenna was fixed at 10 mm away from the head at its largest diameter of 200 mm, while the transmitter was placed further away at a distance of 30 mm from the head. For each transmitting position, the receiver was radially rotated with a step of 15 degrees, measuring the external field of the head at 24 receiving positions. A frequency range of 0.5 to 2.5 GHz was measured for both types of measurements.

To experimentally assess the performance of the two algorithms, we prepared gelatin-oil mixtures derived from the phantom preparation technique that is described in [14], which has been fully analyzed for head tissue mimicking phantoms in [6]. Overall, we prepared mixtures for average brain and blood. Tables 1 and 2 show the concentrations of materials used for each solution and their measured dielectric properties (at 1 GHz), respectively.

Table 1. Quantities of materials used for 100 ml of human tissue mimicking phantoms.

	Average brain	**Blood**
Water	60 ml	80 ml
Gelatin powder	11 gr	16 gr
Kerosene	13 ml	-
Safflower oil	13 ml	-
Propanol	2.5 ml	1.5 ml
Surfactant	4 ml	-

After preparation, the average brain solution was poured into a 3D printed standardized (EN 50361-2001 and IEEE 1528-2003) anthropomorphic head mould of figure 3(a), by slowly pouring it inside, through the hole on the top of the mould. We conducted two sets of measurements, one with

Table 2. Dielectric properties of tissue mimicking phantoms at 1 GHz.

	ε'	ε''
Average brain	41.1	0.35
Blood	62.3	0.56

one layer of average brain ("no target" case) and one with an additional target with blood's dielectric properties ("with target" case). To place the target, after performing the "no-target" measurements we created a slice in the upper part of the mould, by using a thin string and detaching this part (figure 3(b)). Then we used a cylindrical mould to extract a part of the brain and create a cylindrical cavity (diameter = 30 mm) which was filled with the blood target mixture. The target was eccentrically placed 40 mm horizontally and 25 mm vertically from the center of the phantom (figure 3(c)). Lastly, the upper head section was re-attached, and "with target" measurements were performed.

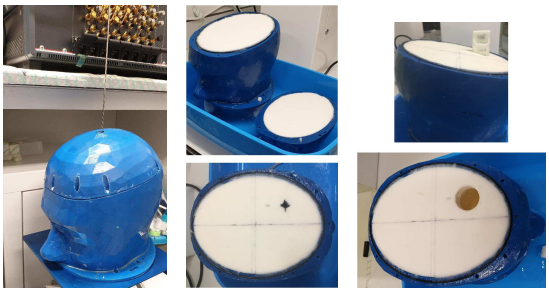

(a) (b) (c)

Figure 3. Anthropomorphic head model and the preparation stages of the phantom layers.

4 Results and discussions

Corresponding to the tomography reconstructions, figure 4 shows the scattered signal difference between the "with target" and "no target" cases, for both antenna types, at 0.7 GHz. The graphs point to better performance of triangular antennas due to larger signal difference, which is confirmed by our resulting reconstructed images through DBIM-TwIST, where the images received when using the triangular antennas indicate better target detection and localization. Figures 5(a), (b) and (c) depict the reconstructed

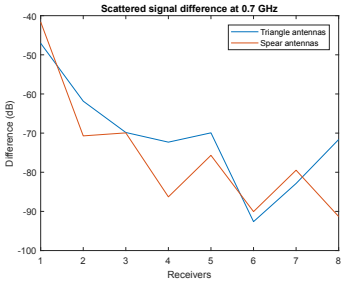

Figure 4. Scattered signal difference between the "with target" and "no target" cases, for the two antennas.

real permittivity for the head model when using the triangular antennas, for three different single frequencies of 0.7, 0.9 and 1.2 GHz, respectively. The dimensions of the reconstruction domain is 202×158 mm for the plastic layer and 170×127 mm for the average brain layer. This corresponds to the dimensions of the phantom's axial slice at the height where the antennas are placed.

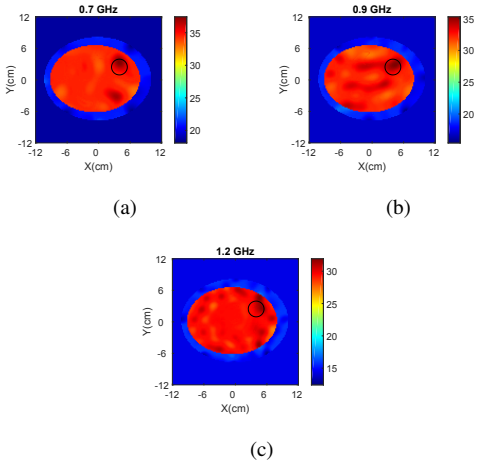

(a) (b)

(c)

Figure 5. Single frequency reconstructions of the real permittivity for (a) 0.7, (b) 0.9, and (c) 1.2 GHz.

Processing the data from the radar measurements indicated a frequency range of 0.65-0.75 GHz as the frequency band with the best performance, with the spear antennas providing better image reconstructions. Figure 6 shows the S-parameter values for this band for both with and without target cases, when the spear antennas are at their nearest distance (S21), 90° apart (S71) and farthest distance (S13-1), respectively. Figures 7(a) and (b) show the normalized intensity images of the head phantom obtained through Huygens algorithm, before and after image adjusting, respectively. It can be seen that the target is detected and localized in its correct position without any artefacts. Image adjustment is performed through forcing to 0 all intensity values above 0.6, and re-scaling the intensity values above 0.6, to better highlight the target in the area of interest.

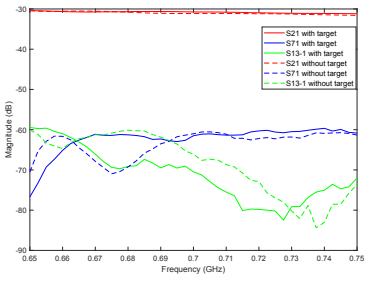

Figure 6. S-parameter magnitude (dB) plot for different antenna distances in the range of 0.65-0.75 GHz.

It should be stated that the exact "no target" reference measurement will not be available in a realistic clinical scenario

for stroke detection, and hence our future simulation and measurements will examine the important challenge of further testing the robustness of our algorithms with respect to the absence of prior information (reference scenario).

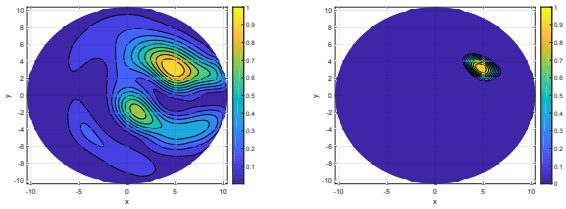

(a) (b)

Figure 7. Intensity images of the phantom (a) before, and (b) after image adjusting; x and y axes are in centimeters.

5 Conclusions

The work on this paper presented for the first time, a qualitative comparison between a tomographic and a radar-based algorithm on data collected from an anthropomorphic head model and a custom-built prototype. Our results show that both algorithms are capable of detecting and localizing the blood mimicking target in its approximate position, through the subtraction between the head with and without the target. The measurements were done using two different antennas, with DBIM-TwIST algorithm showing a better performance with the triangular antenna while the Huygens algorithm worked more optimally with spear antenna. Future work will extend the complexity and the in-homogeneity of the head models. Following the results presented in this paper, we aim to develop a hybrid image processing algorithm, combining the strongest features of both DBIM-TwIST and Huygens methods described in this paper.

6 Acknowledgements

This research was supported in part by UK's Engineering and Physical Sciences Research Council (EPSRC) under project grant EP/R013918/1, and in part by the EMERALD project funded from the European Union's Horizon 2020 under the Marie Sklodowska-Curie grant agreement No. 764479.

References

[1] V. Feigin, "Stroke epidemiology in the developing world," *The Lancet*, **365**, 9478, 2005, pp. 2160–2161.

[2] R. Chandra, H. Zhou, I. Balasingham, and R. M. Narayanan, "On the opportunities and challenges in microwave medical sensing and imaging," *IEEE transactions on biomedical engineering*, **62**, 7, 2015, pp. 1667–1682.

[3] M. Azghani, P. Kosmas, and F. Marvasti, "Microwave medical imaging based on sparsity and an iterative method with adaptive thresholding," *IEEE transactions on medical imaging*, **34**, 2, 2014, pp. 357–365.

[4] R. Scapaticci, et al., "Design and numerical characterization of a low-complexity microwave device for brain stroke monitoring," *IEEE Transactions on Antennas and Propagation*, **66**, 12, 2018, pp. 7328–7338.

[5] Z. Miao, and P. Kosmas, "Multiple-frequency DBIM-TwIST algorithm for microwave breast imaging," *IEEE Transactions on Antennas and Propagation*, **65**, 5, 2017, pp. 2507–2516.

[6] O. Karadima, et al., "Experimental validation of microwave tomography with the DBIM-TwIST algorithm for brain stroke detection and classification," *Sensors*, submitted.

[7] N. Ghavami, J. Sotiriou, and P. Kosmas, 2019, "Preliminary Experimental Validation of Radar Imaging for Stroke Detection with Phantoms," in *42nd Progress In Electromagnetics Research Symposium*. Xiamen, China, 2019.

[8] J. D. Shea, P. Kosmas, S. C. Hagness, and B. D. Van Veen, "Three-dimensional microwave imaging of realistic numerical breast phantoms via a multiple-frequency inverse scattering technique," *Medical physics*, **37**, 8, 2010, pp. 4210–4226.

[9] J. M. Bioucas-Dias, and M. A. Figueiredo, "A new TwIST: Two-step iterative shrinkage/thresholding algorithms for image restoration," *IEEE Transactions on Image processing*, **16**, 12, 2007, pp. 2992–3004.

[10] N. Ghavami, G. Tiberi, D. J. Edwards and A. Monorchio, "UWB Microwave Imaging of Objects With Canonical Shape," *IEEE Transactions on Antennas and Propagation*, **60**, 1, Jan. 2012, pp. 231–239.

[11] N. Ghavami, P. Probert Smith, G. Tiberi, D. Edwards, and I. Craddock, "Non-iterative beamforming based on Huygens principle for multistatic ultrawide band radar: application to breast imaging," *IET Microwaves, Antennas & Propagation*, **9**, 12, 2015, pp. 1233–1240.

[12] W. Guo, S. Ahsan, M. He, M. Koutsoupidou, and P. Kosmas, "Printed monopole antenna designs for a microwave head scanner," *2018 18th Mediterranean Microwave Symposium (MMS)*, Nov. 2018, pp. 384–386.

[13] M. Koutsoupidou, et al, "Towards a microwave imaging prototype based on the DBIM-TwIST algorithm and a custom-made transceiver system," *ICEAA*, Verona, 2017, pp. 1004–1007.

[14] M. Lazebnik, E. L. Madsen, G. R. Frank, and S. C. Hagness, "Tissue-mimicking phantom materials for narrowband and ultrawideband microwave applications," *Physics in Medicine & Biology*, **50**, 18, 2005, pp. 4245.